ARTICLE   OPEN

Machine learning guided high-throughput search of non-oxide garnets

Jonathan Schmidt [1], Hai-Chen Wang[1], Georg Schmidt[1] and Miguel A. L. Marques [1] ✉

Garnets have found important applications in modern technologies including magnetorestriction, spintronics, lithium batteries, etc. The overwhelming majority of experimentally known garnets are oxides, while explorations (experimental or theoretical) for the rest of the chemical space have been limited in scope. A key issue is that the garnet structure has a large primitive unit cell, requiring a substantial amount of computational resources. To perform a comprehensive search of the complete chemical space for new garnets, we combine recent progress in graph neural networks with high-throughput calculations. We apply the machine learning model to identify the potentially (meta-)stable garnet systems before performing systematic density-functional calculations to validate the predictions. We discover more than 600 ternary garnets with distances to the convex hull below $100\ \mathrm{meV \cdot atom^{-1}}$. This includes sulfide, nitride, and halide garnets. We analyze their electronic structure and discuss the connection between the value of the electronic band gap and charge balance.

INTRODUCTION

Garnets can be found throughout the world in diverse geological environments, and have been known since prehistory mainly due to their use in jewelry as gemstones. They are also relatively hard minerals, a property that makes them useful for a series of industrial applications, such as in waterjet cutting or as abrasives.

Generally, the garnets crystallize in a cubic structure (space group $Ia\bar{3}d$) with chemical composition $A_3B_2(B'C_4)_3$, where the A atoms are located in the 24c dodecahedral sites, the B atoms are in the 16a octahedral, and B' atoms occupy the 24d tetrahedral sites. In ternary garnets, B and B' sites are occupied by the same chemical element. Around 1950[1-3] some rare-earth garnets, especially yttrium-based materials, started to attract attention. Those garnets have a general formula of $RE_3B_2(BO_4)_3$ where RE stands for rare-earth and B is a 3d magnetic transition metal (usually iron) or a group IIIA element. Among these, one of the most used ones is yttrium aluminum garnet (YAG), $Y_3Al_2(AlO_4)_3$, used as a synthetic simulant to diamond due to its high refractive index (> 1.8)[4]. Doped YAGs with other rare-earth elements have found numerous applications as lasing media in modern medical laser devices[5] or in tunable optical devices[6-9].

Other important compounds, with interesting ferrimagnetic properties, are the rare-earth iron garnets $(RE_3Fe_2(FeO_4)_3$, RIG). In the RIG structure, five Fe atoms occupy two different sublattices, and the antiferromagnetic coupling between sublattices and ferromagnetic coupling within the sublattice leads to a ferrimagnetic configuration. RIGs can display a rather high Curie temperature (around 560 K[10]), and some systems exhibit giant magnetorestriction[11]. Moreover, RIGs materials have a band gap with values around 2.6 to 2.9 eV[12,13]. Among these materials yttrium iron garnet (YIG) stands out because it has an exceptionally low Gilbert damping. YIG has first been used as bulk material in optical insulators, circulators, and Faraday rotators. Since the last two decades, YIG is also more and more frequently used as thin film material for spintronic applications[14] because it allows the transmission of spin currents although being an insulator by itself. In recent years we have witnessed the attempt

to replace yttrium with lanthanides to increase the spin-orbit coupling and introduce even Dzyaloshinskii-Moriya interactions in hybrid systems.

Another interesting group of quaternary garnets is the lithium garnets $LN_3M_2(LiO_4)_3$, where LN is a lanthanide and M is either Te, Ta, or Nb. With partial Li-filling of the invasive positions of tetrahedral and distorted octahedral sites, the stuffed lithium garnets $(LN_3M_2Li_2(LiO_4)_3)$ have a promising lithium-ion conductivity and chemical stability, showing potential as solid electrolytes in Li-batteries[15,16].

The many applications of garnets, and of YIG in particular, has increased the need for garnets with different properties. Unfortunately, the deposition of garnet thin films with high quality is only possible on garnet substrates due to the special crystal structure[17-19]. Moreover, for spintronics applications, it would be a huge step forward to be able to pair, for example, thin YIG films in hybrid structures with other conducting films being either metallic or having such a low band gap that reasonable electron conductivity is achievable at room temperature[17-19]. Again to achieve a perfect interface in these structures one would need to create an all-garnet hybrid which is currently prevented by the obvious lack of room-temperature conducting or metallic garnets. Such a material class would dramatically extend the applicability of garnet thin films.

However, despite these diverse applications and the technological relevance of garnets, most of the research in garnets is confined to oxides[20], and only a few halides (also called cryolithionites) are known experimentally[21]. This is can be easily understood, as oxides are usually simpler to work with under ambient experimental conditions. Furthermore, a computational high-throughput search of new compositions for the garnet prototype is challenging, as the garnet cubic primitive unit cell contains 80 atoms, which is an order of magnitude larger than most structure prototypes used in recent high-throughput searches such as (double-)perovskites[22,23], (half-)Heuslers[24], dichalcogenides[25], etc.

---

[1]Institut für Physik, Martin-Luther-Universität Halle-Wittenberg, D-06099 Halle, Germany. ✉email: miguel.marques@physik.uni-halle.de
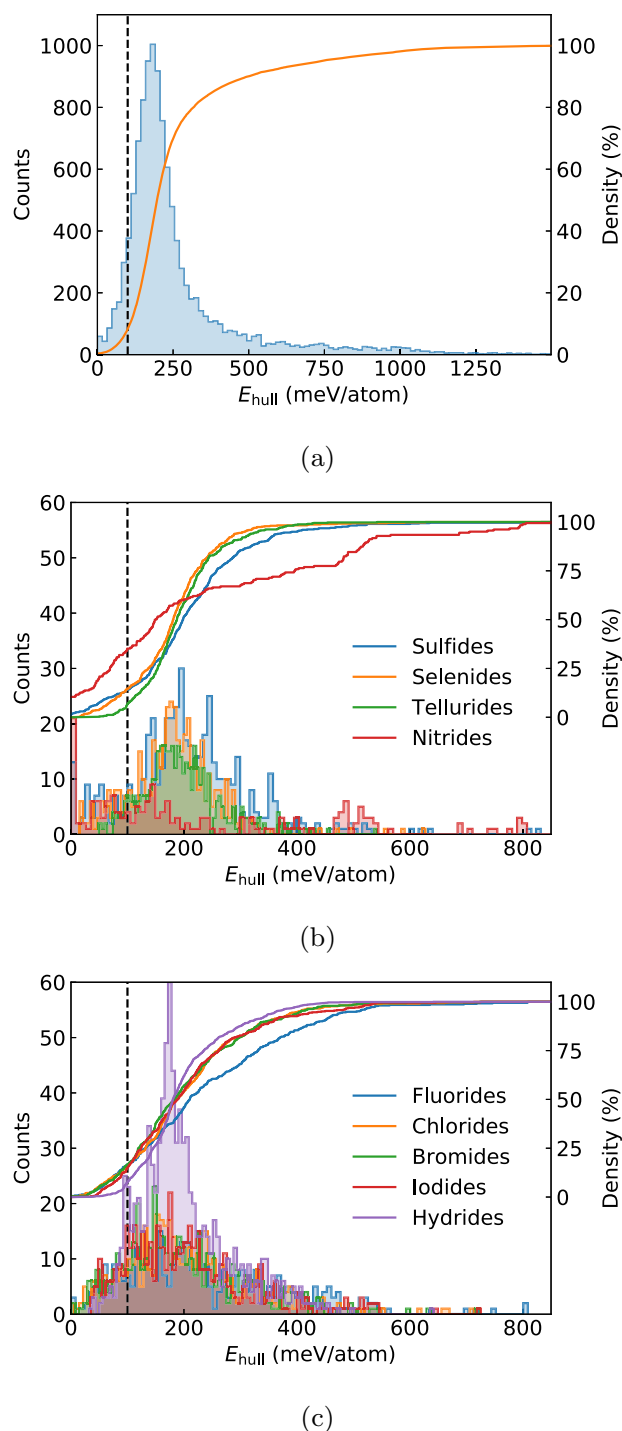
Fig. 1 **The distribution of the distance to the convex hull (E_{hull}).** **a** All calculated compositions and various garnet groups. The panels show histograms of the DFT distance to the convex hull. The first panel shows all data while the latter two show, respectively, **b** chalcogenides and nitrides, and **c** halides and hydrides. The cutoff to filter (meta-)stable systems ($100 \, meV \cdot atom^{-1}$) is shown as a dashed vertical line.

Fortunately, with the aid of state-of-the-art machine learning techniques, the problem of searching through the entire combinatorial chemical space can be significantly accelerated. With pre-trained machine models, we can filter millions of compositions according to the predicted stability without performing costly density-functional theory (DFT) calculations for all the compositions. Nevertheless, DFT validation of the stable compounds is still necessary as a post-processing step.

In the present paper, we followed such a procedure to explore possible (meta-)stable compounds beyond oxy-garnets. The rest of the paper is structured as follows. In "Methods", we explain the machine learning model and the computational methods we applied. In "Results and discussion", we present the most interesting crystal phases we uncovered in our work and discuss the potential applications of the new proposed compounds. Finally, we present our conclusions and an outlook.

RESULTS AND DISCUSSION

Stability and chemistry
In total, the machine-learning model predicted around 12300 compositions below $200 \, meV \cdot atom^{-1}$ from the convex hull of thermodynamic stability that was not present in the Materials Project database[26] nor in the Inorganic Crystal Structure Database[27] (ICSD). All these calculations can be downloaded from the Materials Cloud repository[28]. The cutoffs of $100 \, meV \cdot atom^{-1}$ and $200 \, meV \cdot atom^{-1}$ were chosen based on the fact that ~20% of the experimentally realized materials, present in the materials project database, have a distance to the convex hull larger than $100 \, meV \cdot atom^{-1}$. Note that this, however, does not mean that 20% of materials above 100 meV/atom can be synthesized, as this value represents a conditional probability and not an absolute one. As such, the probability that a material can be synthesized decreases very rapidly with the distance to the hull, and is very small for a compound 200 meV/atom above it. Therefore, the priority for experimental synthesis should be compounds on the hull or very close to it. As the CGAT model has its own errors we doubled the cutoff for the machine learning predictions. The influence of this cutoff is also further discussed in the Supplementary Information.

After the DFT validation calculations, we re-evaluated the distance to the convex hull (E_{hull}) of these candidates using the much more complete convex hull of ref. [29]. The convex hull from ref. [29] includes all stable compounds from the whole materials project, a subset of AFLOW, and millions of our own calculations. This results in 63804 compounds from the DCGAT database and 5291 compounds from AFLOW and the materials project. Naturally, even this convex hull is not complete, therefore these predictions are less precise for some compositions. The decomposition channels for the materials are also denoted in the Supplementary Information. The histogram of the values E_{hull} is shown in Fig. 1a. We also separate the systems into sulfides, selenides, tellurides, nitrides, chlorides, bromides, iodides, and hydrides. These comprise the majority of all systems found. Most of the candidates have an E_{hull} larger than $100 \, meV \cdot atom^{-1}$, but there are still more than one thousand (~9%) compositions below this threshold. The high-throughput success rate, that we define by the number of compounds that are within $100 \, meV \cdot atom^{-1}$ from the convex hull divided by the total number of DFT calculations, stood at 14%, with a maximum of 35% for nitrides and a minimum of 8% for hydrides. These numbers prove the efficiency of our machine-learning-assisted high-throughout search. The histogram of E_{hull} for these categories as well as all calculated compositions are shown in Fig. 1.

The distribution of E_{hull} for all systems follows the typical skewed Gaussian with the peak located at around $200 \, meV \cdot atom^{-1}$ and a fat tail that extends beyond 1 eV/atom, in agreement with the MAE errors for our machine-learning models. Individual distributions for chalcogenides are also skewed Gaussians peaking at around $200 \, meV \cdot atom^{-1}$. The amount of (meta-)stable compounds decreases from sulfides to tellurides, which is also expected as this is the common trend of stability for

Table 1. Number of (meta-)stable systems (N_{stable}) below $100\,meV \cdot atom^{-1}$ from the convex hull of thermodynamic stability and high-throughput success rate (R) for each category.

Category	N_{stable}	R (%)
Sulfides	70	14
Selenides	68	15
Tellurides	28	7
Nitrides	64	35
Fluorides	62	17
Chlorides	68	16
Bromides	72	17
Iodides	68	15
Hydrides	69	8
Total	569	14

Table 2. The calculated lattice constant (a, in Å), band gap calculated with PBE (Gap^{PBE}) and MBJ (Gap^{MBJ}) functional (in units of eV), distance to the convex hull (E_{hull} in $meV \cdot atom^{-1}$), effective electron (m_e^*) and hole (m_h^*) masses (in units of m_e^0), for some selected (meta-)stable sulfide and nitride garnets, data for $Y_3Al_5O_{12}$ is also listed for comparison.

Formula	a	Gap^{PBE}	Gap^{MBJ}	E_{hull}	m_e^*	m_h^*
$Y_3Al_5O_{12}$	12.125	4.53	6.12	0	1.3	6.8
$Y_3Al_5S_{12}$	14.932	2.08	3.00	1	0.7	1.5
$Y_3Ga_5S_{12}$	15.073	1.32	2.45	46	0.5	3.2
$Y_3In_5S_{12}$	15.709	1.35	2.38	46	0.5	2.6
$Y_3Al_5Se_{12}$	15.752	1.45	2.15	36	0.5	1.5
$Y_3Al_5Te_{12}$	17.120	0.60	1.07	84	0.3	2.7
$Y_3Ge_5S_{12}$	15.324	0.00	0.00	81	–	–
$Ca_3W_5N_{12}$	12.928	0.93	1.57	0	0.9	3.2
$Ca_3Re_5N_{12}$	12.896	0.00	0.00	9	–	–
$La_3Nb_5N_{12}$	13.297	0.00	0.00	99	–	–
$K_3In_5F_{12}$	14.898	2.41	3.39	59	0.8	6.1
$K_3In_5I_{12}$	19.977	0.00	0.00	61	–	–
$Mg_3Rh_5H_{12}$	11.008	0.00	0.00	51	–	–
$Y_3Rh_5H_{12}$	11.581	0.00	0.00	93	–	–

the chalcogenides. Unlike the situation for chalcogenides, the distribution curve for nitrides has multiple peaks, and shows that there are plenty of potentially stable nitride garnets. For halides and hydrides the histograms are again skewed Gaussian similar to those of chalcogenides, but there is no clear trend in what concerns stability across the group. For hydrides, the total number of systems is much larger, but a lower percentage of them are (meta-)stable compared to the halides.

The total number of (quasi-)stable systems for each category is listed in Table 1. A full list of the systems can be found in Supplementary Table 2. We also selected a dozen of them to analyze more closely in Table 2. Later discussions will mainly focus on these systems.

From our calculations, we recover the majority of the oxide garnets that are already known experimentally, but we also obtain a wealth of different compounds not present in available databases. Of 27 ternary garnets with the composition $A_3B_5C_{12}$ present in the ICSD (prototypes Garnet(YAG)#$Y_3Al_5O_{12}$ and Garnet#$Ca_3Al_2(SiO_4)_3$) we recover 22. Three of those missed contained Yb which we removed from our predictions due to convergence issues with that chemical element. The two remaining garnets we missed were $Fe_5Si_3O_{12}$ and $Mn_5Si_3O_{12}$ (although we did discover $Mn_3Si_5O_{12}$). Many of these systems are oxides, that have been the subject of a recent high-throughput search[20] with results similar to ours. Interestingly, we also find a wealth of other chalcogenides, nitrides, halides, and even hydrides as shown in Fig. 1b, c and in Table 1.

From the stable compounds, several are closely related to the oxide garnets by the chemical substitution of oxygen by another chalcogen. These garnets along with their counterparts are presented in Table 3. The existence of such compounds is expected due to the chemical similarity among chalcogens. In those chalcogenides, the dodecahedral sites (site A in $A_3B_5C_{12}$) are mostly occupied by rare-earth elements, and according to the element occupying the octahedral and tetrahedral sites (site B), the chalcogenides can be further divided into several categories. The numbers of (meta-)stable systems for each category decrease in the following order: occupying B with group IIIA elements (Al, Ga, In, Tl), group IVA elements (Ge, Sn, Pb), group VA elements (As, Sb, Bi), and transition metals (Ag, Cu, Sc, Ti). The preference of group IIIA elements for site B can be understood by simple charge compensation arguments. The most common oxidation state of the chalcogens is -2, while the rare-earth elements in sites A are $+3$: the composition reaches the 'balanced' or 'compensated' state if B is in the oxidation state $+3$. Moreover, for balanced $A_3^{III}B_5^{III}C_{12}^{-II}$ chalcogenide compositions, one would expect the compounds to be semiconductors. This is indeed what we find (see an example in "Electronic structure"). We also analyzed the

correlation between the band gap and all standard stochiometric and ionic features of matminer[30] and found that for all correlation coefficients (Pearson, Spearman, ϕ_k) only the feature 'compound possible' was significantly correlated with the band gap. This feature describes if the material is likely to be charge neutral according to the oxidation state or not. Besides the chalcogenides, we discover 64 stable nitrides as seen in Table 1. As discussed above, to reach a balanced oxidation state, elements with higher oxidation state should be favored to combine with -3 oxydation state of nitrogen. Indeed for nitride garnets $A_3B_5N_{12}$, position A is mostly occupied by $+2$ or $+3$ chemical elements, and for position B the majority of meta-stable systems have elements with oxidation state $+6$ (Mo and W). Although a $+6$ element is required to achieve a balanced state, we also find that relatively stable compounds are possible for $+5$ (Nb and Ta), and $+7$ (Re). We could argue that the balanced nitrides should be semiconducting. However, due to the low electronegativity of nitrogen the gap may close (see one such example in "Electronic structure").

We can also identify several halides and hydrides from Fig. 1c. However, halogens (and hydrogen in hydrides) have an oxidation state of -1, which makes it more difficult to reach a balanced oxidation state with the $A_3B_5C_{12}$ stoichiometry. One viable scheme is with an A element that is $+1$, while the B elements in 16a and 24d Wycoff positions are respectively $+3$ and $+1$, i.e., having the form of $A_3^I B_2^{III}(B^I C_4^{-1})_3$. Chemical elements exhibiting both $+1$ and $+3$ oxidation states are quite rare. Nevertheless, we still discovered some meta-stable semiconducting halide garnets, for example, $K_3In_5F_{12}$.

There are other compositions that do not belong to any of the discussed classes, such as for example $Sr_{12}Zn_3H_5$. Most of them are 'inverted'-garnets, i.e., with cations instead of anions occupying the C-sites, and have a comparatively higher E_{hull} than regular garnets. Furthermore, only a few anti-garnets with the A and B sites both occupied by the chemical elements of the nitrogen group could potentially become oxidation state balanced.

We have to again emphasize that, in order to form (meta-)stable or insulating/semiconducting compounds, charge compensation is neither a necessary nor a sufficient condition, and we find many exceptions in Supplementary Table 2. However, it gives us a simple, intuitive argument to understand why a system is

Table 3. The experimentally known oxy-garnets (not including 3d metals in the B sites), their ICSD ID, Materials Project ID, and predicted meta-stable counterparts with different C anions.

Formula	ICSD ID	MP ID	Counterparts
$Y_3Al_5O_{12}$	20090, 41144, 41145, 67102, 67103, 93634, 93635, 170157, 170158, 236589, 280104, 17687, 17688, 17689, 17690, 74607, 31496	mp-3050	$Y_3Al_5S_{12}(1)$; $Y_3Al_5Se_{12}(36)$; $Y_3Al_5Te_{12}(84)$
$La_3Al_5O_{12}$		mp-780432	$La_3Al_5S_{12}(0)$; $La_3Al_5Se_{12}(18)$; $La_3Al_5Te_{12}(49)$
$Eu_3Al_5O_{12}$	245326	mp-21757	$Eu_3Al_5S_{12}(58)$; $Eu_3Al_5Se_{12}(88)$
$Tb_3Al_5O_{12}$	33602	mp-14387	$Tb_3Al_5S_{12}(0)$; $Tb_3Al_5Se_{12}(29)$; $Tb_3Al_5Te_{12}(80)$
$Er_3Al_5O_{12}$	170147, 280606, 170146, 62615	mp-3384	$Er_3Al_5S_{12}(8)$; $Er_3Al_5Se_{12}(50)$; $Er_3Al_5Te_{12}(98)$
$Gd_3Al_5O_{12}$	192184	mp-14133	$Gd_3Al_5S_{12}(0)$; $Gd_3Al_5Se_{12}(21)$; $Gd_3Al_5Te_{12}(63)$
$Ho_3Al_5O_{12}$	409390, 33603	mp-14388	$Ho_3Al_5S_{12}(5)$; $Ho_3Al_5Se_{12}(44)$; $Ho_3Al_5Te_{12}(92)$
$Lu_3Al_5O_{12}$	259144, 17789, 182354	mp-14132	$Lu_3Al_5S_{12}(27)$; $Lu_3Al_5Se_{12}(70)$
$Y_3Ga_5O_{12}$	80148, 14343, 185862, 23852	mp-5444	$Y_3Ga_5S_{12}(46)$; $Y_3Ga_5Se_{12}(81)$
$La_3Ga_5O_{12}$		mp-780561	$La_3Ga_5S_{12}(36)$; $La_3Ga_5Se_{12}(54)$
$Tb_3Ga_5O_{12}$	20831, 84875, 184934	mp-5965	$Tb_3Ga_5S_{12}(45)$; $Tb_3Ga_5Se_{12}(74)$
$Sm_3Ga_5O_{12}$	9236, 84873, 291192	mp-5800	$Sm_3Ga_5S_{12}(37)$; $Sm_3Ga_5Se_{12}(63)$; $Sm_3Ga_5Te_{12}(98)$
$Nd_3Ga_5O_{12}$	84872	mp-15239	$Nd_3Ga_5S_{12}(33)$; $Nd_3Ga_5Se_{12}(56)$; $Nd_3Ga_5Te_{12}(98)$
$Gd_3Ga_5O_{12}$	9237, 37145, 192181, 84874, 184931	mp-2921	$Gd_3Ga_5S_{12}(32)$; $Gd_3Ga_5Se_{12}(66)$; $Gd_3Ga_5Te_{12}(93)$
$Lu_3Ga_5O_{12}$	23850	mp-14134	$Lu_3Ga_5S_{12}(73)$
$Dy_3Ga_5O_{12}$	409391	mp-15576	$Dy_3Ga_5S_{12}(48)$; $Dy_3Ga_5Se_{12}(80)$
$Er_3Ga_5O_{12}$	9238	mp-12236	$Er_3Ga_5S_{12}(54)$; $Er_3Ga_5Se_{12}(94)$
$Ho_3Ga_5O_{12}$	409390	mp-15575	$Ho_3Ga_5S_{12}(51)$; $Gd_3Ga_5Se_{12}(88)$

The distance to the hull calculated with DFT is in parentheses (in $meV \cdot atom^{-1}$).

stabilized or has an electronic band gap. Furthermore, we have to keep in mind that uncompensated systems might be further stabilized through defects, such as vacancies. To simplify our discussion, we leave such possibilities to future works and focus the following on (meta-)stable regular garnet systems which could have balanced charges, specifically chalcogenides (except oxides), halides, hydrides, and nitrides.

Another important point regards the dynamic stability of the predicted structures. To investigate this issue we calculated the phonon frequencies at Γ for a few representative materials, specifically $Y_3Al_5S_{12}$, $Y_3Ga_5S_{12}$, $Y_3Ge_5S_{12}$, $Y_3Al_5Se_{12}$, $Y_3Al_5Te_{12}$, $K_3In_5F_{12}$, $K_3In_5I_{12}$, $Mg_3Rh_5H_{12}$, and $Ca_3Re_5N_{12}$. The sulfide, the selenide, and the telluride systems are dynamically stable, however, the fluoride, iodide, hydride, and nitride exhibited imaginary phonon frequencies. We rattled the initial structures, breaking all internal symmetries, and re-optimized them. We found overall relatively small changes in the geometry, linked to distortions of the octahedra and the tetrahedra, leading to minute decreases of the total energy smaller than $30\,meV \cdot atom^{-1}$.

Electronic structure

We illustrate the possible electronic structures of our garnets through a few selected examples depicted in Figs. 2–4.

Generally, the electron states around the Fermi level in garnets can be classified into three categories: (i) from s–p, p–p, or even d–p bonding orbitals between B and C atoms, (ii) from corresponding anti-bonding between B and C atoms, and, (iii) from d-electrons from A atoms if these are d-block or f-block metals. From the simplest tight-binding model, and as expected

from $k \cdot p$ theory, we know that the larger the difference between the electronegativity of B and C and the shorter B–C bond-length, the larger the separations between states (i) and (ii). For the d (or f) block elements occupying the A-site, the position of states (iii) can be between (i) and (ii), overlapping with, or even above the latter. In charge compensated situations, the bands (i) are completely filled, while (ii) and (iii) (if applicable) bands are empty, resulting in insulating/semiconducting systems. Otherwise, depletion of bands (i) or filling of bands (ii) or (iii) can happen, leading to metallic systems. Although many deviations from this simple tight-binding picture appear, we will see how these general patterns are useful to understand the band-structures.

For chalcogenide garnets, we chose as representative examples $Y_3Al_5S_{12}$, $Y_3Ge_5S_{12}$, and $Y_3Ga_5S_{12}$, while more examples can be found in the Supplementary Information. The band structures of these compounds are shown in Fig. 2, together with $Y_3Al_5O_{12}$ for comparison. The oxidation state balanced $Y_3Al_5CH_{12}$ (CH = S, Se, Te) garnets are semiconductors as expected. For $Y_3Al_5S_{12}$ the band structure is shown in Fig. 2b. Similar to its oxide counterpart in Fig. 2a, the Y–d states dominate the conduction bands (CB) slightly hybridizing with Al(p) and S(p)-states. These bands are from the type (iii) states as discussed above. The valence bands (VB) around Fermi level are mainly composed of the localized anionic p–states of type (i), also representing the typical situation described above. From $Y_3Al_5O_{12}$ to $Y_3Al_5Te_{12}$ (see Supplementary Fig. 2), following the decreasing trend of electronegativity for chalcogens, the band gap shrinks and the band edges become more dispersed.

The elements occupying the B position in charge compensated chalcogenides also have a crucial effect on the electronic structure. For example, $Y_3B_5S_{12}$ (B = Al, Ga, In, Tl, see Supplementary Fig. 2)

(a) $Y_3Al_5O_{12}$

(b) $Y_3Al_5S_{12}$

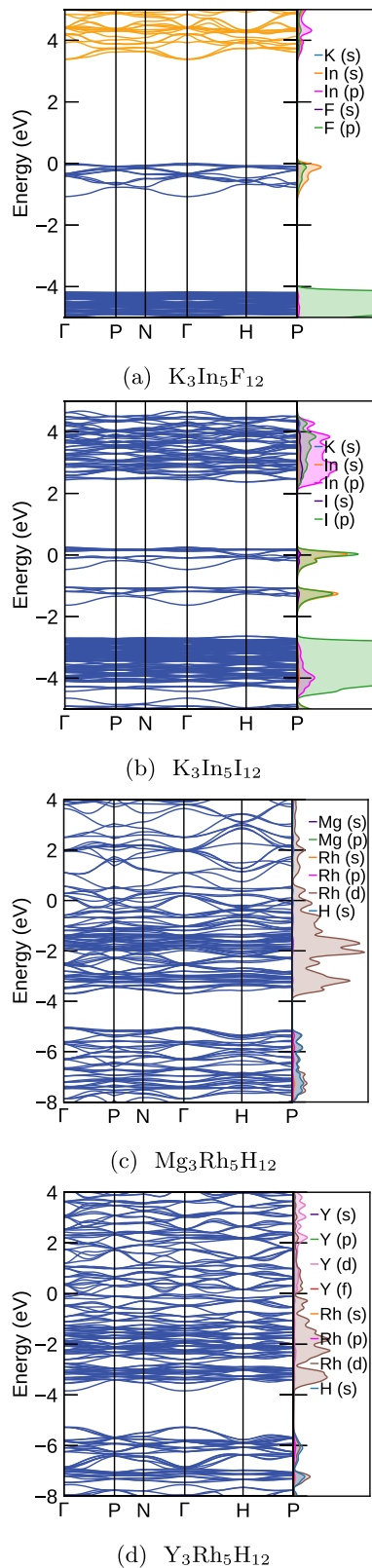(c) $Y_3Ge_5S_{12}$
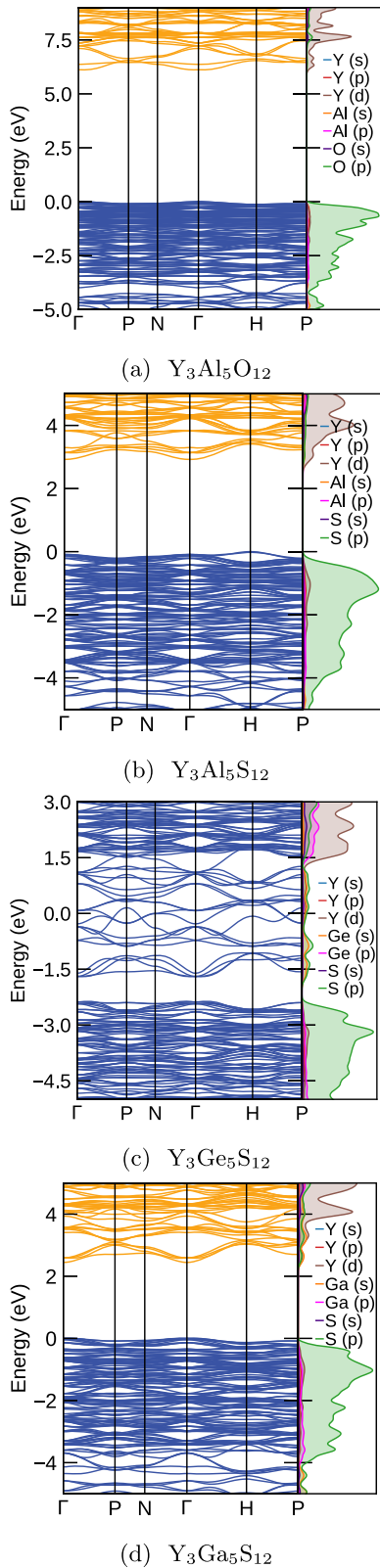
(d) $Y_3Ga_5S_{12}$

Fig. 2 Calculated mBJ electronic band structures for selected chalgogenide garnets. The Fermi level is set at zero. **a** The mBJ electronic band structure of $Y_3Al_5O_{12}$, **b** $Y_3Al_5S_{12}$, **c** $Y_3Ge_5S_{12}$, **d** $Y_3Ga_5S_{12}$.

(a) $Ca_3W_5N_{12}$
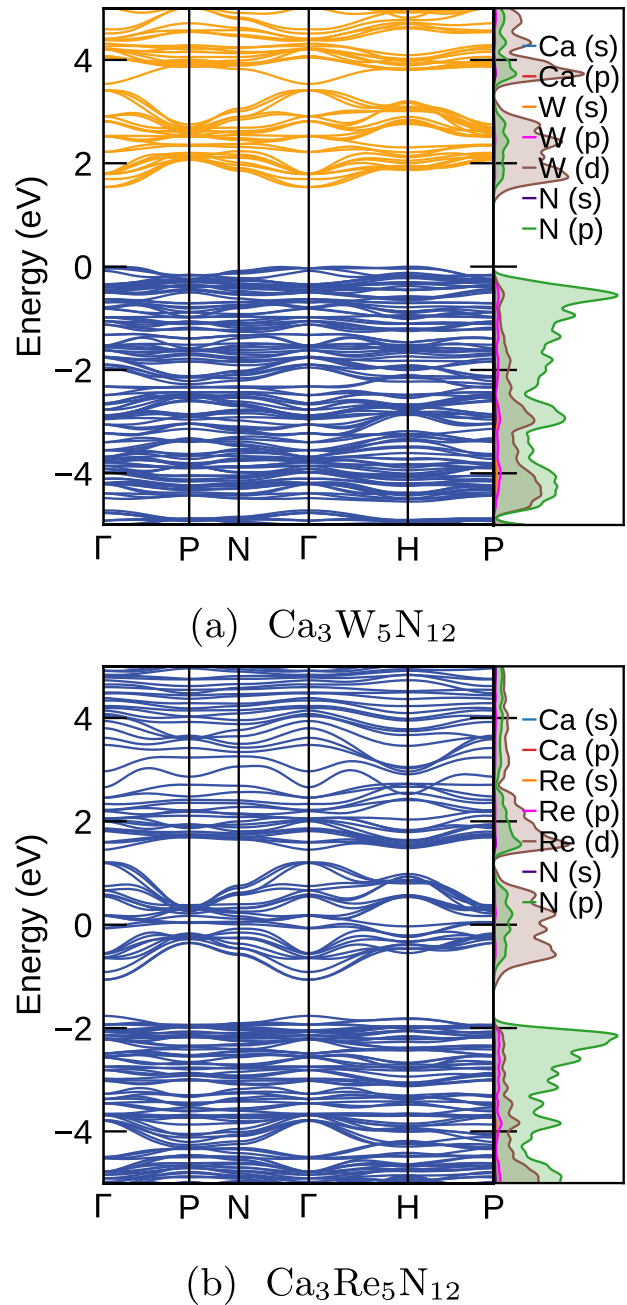
(b) $Ca_3Re_5N_{12}$

Fig. 3 Calculated mBJ electronic band structures for selected nitride garnets. The Fermi level is set at zero. **a** The mBJ electronic band structure of $Ca_3W_5N_{12}$, and **b** $Ca_3Re_5N_{12}$.

all have a direct gap at Γ with the sole exception of $Y_3Al_5S_{12}$ which has an indirect H–Γ gap. Moreover, going from Al to Tl the gap decreases, while the contibution of the s-states from the B atoms to the bottom of the conduction bands increases, leading to more extended bands and lower effective electron masses. Furthermore, for $Y_3Tl_5S_{12}$ we can see that the Y(d) bands are above the Tl(s)-S(s) displaying more disperse anti-bonding mixing, an resulting in very low electron effective masses ($m_e^* = 0.19$).

For chalcogenides with unbalanced oxidation states, such as $Y_3Ge_5S_{12}$, similar features can also be observed (see Fig. 2c). Between the empty Y(d)-S(p) hybridization states of type (iii) and the full S(p) dominated type (i) bands are the states from Ge(s) and S(p) anti-bonding of type (ii). As discussed above they are partially occupied, so the system is metallic. It is possible that the system might re-

(a) $K_3In_5F_{12}$

(b) $K_3In_5I_{12}$

(c) $Mg_3Rh_5H_{12}$

(d) $Y_3Rh_5H_{12}$

Fig. 4 Calculated mBJ electronic band structures for selected halide and hydride garnets. The Fermi level is set at zero. **a** The mBJ electronic band structure of $K_3In_5F_{12}$, **b** $K_3In_5I_{12}$, **c** $Mg_3Rh_5H_{12}$, and **d** $Y_3Rh_5H_{12}$.

establish a balanced oxidation state by creating Ge vacancies thus becoming semiconducting, though a detailed investigation of such a possibility is beyond the scope of the present paper.

Some representatives of the band structures for nitrides garnets are shown in Fig. 3. The oxidation state compensated $Ca_3W_5N_{12}$ is semiconducting. The anti-bonding $p-d$ bands forming the CB also separate into two manifolds: the lower part is mainly constructed from the tungsten on the tetrahedral sites, and the upper part is mainly from the octahedral W. The VB are, as usual, mostly composed of N(p) states. For charge-unbalanced nitrides (such as $Ca_3Re_5N_{12}$) that have more valence electrons from Re compared to W, the Fermi level passes through the partially occupied $p-d$ anti-bonding bands and the system becomes metallic. However, the separation between $p-d$ bonding and anti-bonding bands can still be seen as well as the double manifolds of $p-d$ anti-bonding states. When a chemical element with less valence electrons replaces W, for example, in $La_3Nb_5N_{12}$ (see Supplementary Fig. 2), the minority spin channel of $p-d$ bonding states is partially empty, and the system actually becomes a half-metal.

For halides, we show the band structure of $K_3In_5F_{12}$ and $K_3In_5I_{12}$ as examples. Apparently, the former compound has unbalance oxidation states, however, it is semiconducting. The Bader net charges of the In at octahedral and tetrahedral sites are +1 and +2.4, respectively. The In in the B-site is therefore in the +1 and +3 oxidation states, reaching charge compensation as discussed above. The top of the valence bands are mainly composed of In(s)-F(p) anti-bonding states, which separate from the lower valance bands, formed by localized F(p)-In(p) bonding states, by around 4 eV. Unlike in most sulfides and nitrides, where d-states from A atoms dominate the bottom of the conduction bands, in $K_3In_5F_{12}$ the bottom of the CB is mainly formed by In(p)-F(p) anti-bonding hybridized states. This is because the K(s)-F(p) anti-bonding states have much higher energy than d-p anti-bonding states in those sulfides and nitrides. When replacing F with I, the Bader net charges for the In atoms in octahedral and tetrahedral sites are respectively +0.7 and +1.0, showing that the +1/+3 oxidation states are not possible in $K_3In_5I_{12}$, and the system becomes metallic. The top valence band formed by In(p)-I(s) anti-bonding states separates in two manifolds. The upper part comes from the In atoms in tetrahedral sites and the lower belongs to the octahedral ones. This can be partially explained by the fact that the In–I bond-length is larger in the latter.

In Fig. 4, we show the band structure of selected examples of hydride garnets. For both $Mg_3Rh_5H_{12}$ and $Y_3Rh_5H_{12}$ the separation between H(s)-Rh(d) mixed bands and cation Rh(d) dominated bands are still present, similar to the situations in other uncompensated garnets. These two systems are also both charge uncompensated, the 'extra' electrons partially filling the Rh(d) dominated bands, leading to metallic systems. Another way to re-establish compensation might be to force more H atoms to occupy the interstitial sites, but again, we leave the exploration of this possibility to future investigations.

In summary, we performed a machine-learning-assisted high-throughput investigation of ternary garnets. We concentrated in non-oxides (that have been studied previously) and in ferromagnetic or paramagnetic compounds. We find a wealth of systems on the convex hull (i.e., thermodynamically stable) or close to it. This includes chalcogenides (with the stability decreasing from S to Te), nitrides, halides, hydrides, etc. We also found other possibilities, such as 'inverted' garnets, but these were slighlty less stable than the conventional phase. The materials tend to be semiconducting/insulating when the composition is charge compensated, otherwise we obtain metallic ground-states. The latter ones could be especially relevant as, to out knowledge, no garnets conducting at room temperature are known. Some of the metallic garnets even have lattice constants that are suitable to create hetero-structures with YIG.

A few chalcogenide garnets, in particular the sulfides, are thermodynamic stable, and are straightforward generalizations of

common oxide garnets. Band gaps are as expected considerably smaller for the sulfides, and decrease further across the periodic group. This opens up the possibility to engineer the band gap of garnets by anionic alloying, from the extreme ultaviolet of the oxide phase to UV-A regime or even into the visible. We predict several nitride systems that have interesting electronic properties due to the presence of transition metals in very high charge states. In view of the recent synthesis of two exotic nitride perovskites[31,32] that were predicted[33,34] with a method similar to the one used in this paper, we are confident that also nitride garnets are accessible experimentally. Finally, we find a few semiconducting halides where the chemical element occupying the octahedral and the dodecahedral site are in two different charge states.

Above all, we believe that our work proves that an exhaustive survey of the ternary, and perhaps also of the quaternary, space of materials is now accessible to high-throughput studies, even for large and complex unit cells. This is made possible by machine learning methods, that already achieved outstanding maturity in the short time since their first appearance, and that is reaching unprecedented accuracy. We expect these methods to further accelerate the discovery of materials with exceptional properties.

METHODS

Machine-learning model

In this work, we applied crystal graph attention networks, developed and pre-trained in ref. [22], to predict thermodynamically stable materials. The networks use an attention-based message-passing approach based on the crystal graph representation of the crystal structure. Replacing the normal distance information that is typically used as edge-representation in crystal graph networks with solely the graph distance of the atoms to their neighbors allows for precise predictions of unrelaxed structures. As garnets crystallize in a cubic structure the list of neighbors and consequently the graph distances are mostly constant throughout the geometry relaxation. This removes the need to perform predictions with multiple cell constant ratios. In the following, we give a short description of CGATs following the notation in ref. [22]. The i_{th} node, i.e., atom, at timestep t of the message passing process will be denoted as h_i^t and the corresponding edge to the atom j as e_{ij}^t. In general, we can summarize the message passing and update equation as follows:

$$\mathbf{h}_i^{t+1} = U\left(\mathbf{h}_i^t, \left\{\mathbf{h}_j^t, \mathbf{e}_{ji}^t\right\}, j \in \mathcal{N}(i)\right). \tag{1}$$

The neighborhood $\mathcal{N}(i)$ of the i_{th} node is determined through a cutoff radius and a maximum number of neighbors within that cutoff radius. The closest neighbors are prioritized when the maximum number of neighbors is reached. We input a concatenation of the previous node and edge embeddings into two fully connected networks that respectively determine the attention vectors $\mathbf{a}_{ij}^{tn}$ and the messages $\mathbf{m}_{ij}^{tn}$. N networks for messages and attention coefficients, i.e. attention heads, are used in parallel. $FCNNN_a^{t,n}$ will be the label of the network of the n_{th} attention head at timestep t.

$$\mathbf{s}_{ij}^{t,n} = FCNNN_a^{t,n}(\mathbf{h}_i^t||\mathbf{h}_j^t||\mathbf{e}_{ij}) \tag{2}$$

$$\mathbf{a}_{ij}^{t,n} = \frac{\exp\left(s_{ij}^{t,n}\right)}{\sum_j \exp\left(s_{ij}^{t,n}\right)} \tag{3}$$

$$\mathbf{m}_{ij}^{t,n} = FCNN_m^{t,n}\left(\mathbf{h}_i^t||\mathbf{h}_j^t||\mathbf{e}_{ij}\right). \tag{4}$$

$$\mathbf{h}_i^{t+1} = \mathbf{h}_i^t + HFCNN_{\theta_g^t}^t\left(\frac{1}{N}\sum_n\sum_j \mathbf{a}_{ij}^n \mathbf{m}_{ij}^n\right). \tag{5}$$

We combine the messages weighted by the attention coefficients through a sum and then average the attention heads in eq. (5). We

enter the resulting vector into a network computed by a hypernetwork. The input to the hypernetwork is the difference between the starting node representation and the node representation at timestep t. To update the edges we use analogous equations:

$$\mathbf{s}_{ij}^{e,n} = FCNNN_a^n\left(\mathbf{h}_i^t||\mathbf{h}_j^t||\mathbf{e}_{ij}^t\right) \tag{6}$$

$$\mathbf{a}_{ij}^{e,n} = \frac{\exp(\mathbf{s}_{ij})}{\sum_n \exp(\mathbf{s}_i^n)} \tag{7}$$

$$\mathbf{m}_{ij}^{e,n} = FCNNN^n\left(\mathbf{h}_i^t||\mathbf{h}_j^t||\mathbf{e}_{ij}^t\right) \tag{8}$$

$$\mathbf{e}_{ij}^{t+1} = \mathbf{e}_{ij}^t + FCNN_{\theta_g^t}^{n,t}\left(\left|\right|_n \mathbf{a}_{ij}^{e,n}\mathbf{m}_{ij}^{e,n}.\right) \tag{9}$$

We concatenate each of the final atomic representations with a global context vector computed by a ROOST[35] model and then combine them through a last attention layer. Finally, a residual network computes the target quantity. The following hyperparameters were used by the networks: optimizer: AdamW; learning rate: 0.000125 (1.5e-05 for transfer learning); starting embedding: matscholar-embedding; nbr-embedding-size: 512; msg-heads: 6; batch-size: 512 (64 transfer learning); max-nbr: 24; epochs: 390; loss: L1-loss; momentum: 0.9; weight-decay: 1e-06; atom-fea-len: 128; message passing steps: 5; roost message passing steps: 3; other roost parameters: default; vector-attention: True; edges: updated; learning rate: cyclical; learning rate schedule: (0.1, 0.05); learning rate period: 130; hypernetwork: 3 hidden layers, size 128; hypernetwork activ. funct.: tanh; FCNN: 1 hidden layer, size 512; FCNN activ. funct.: leaky RELU[36].

Concerning transfer learning, we continue to train all weights of the original model using this dataset with a training/validation/testing split of 80%/10%/10% and a learning rate of 0.000015. The checkpoint with the best validation error from 390 epochs of training is chosen.

In total we repeated the cycle three times. In the first, we performed DFT calculations for 3320 compounds. The mean absolute error (MAE) of the initial pre-trained machine was 0.497 eV/atom. This is a very high value, that was expected as there were very few garnets in the dataset used in ref. [22], and they spanned a very small chemical space. In the second cycle, we validated 7336 compounds, and the transfer-learning model performed much better, with an MAE of 0.064 eV/atom. Finally, in the third cycle, we computed 3844 materials with DFT. The final model had an MAE of 0.058 eV/atom, showing that the transfer-learning workflow is meaningful and converges quickly.

DFT calculations

We perform DFT calculations using the package VASP with PAW[37] datasets of version 5.2., as recommended by the materials project, and with the Perdew-Burke-Ernzerhof[38] (PBE) exchange-correlation functional. Following the Materials Project[26] recommendations, we use extra on-site corrections for oxides, fluorides containing Co, Cr, Fe, Mn, Mo, Ni, V, and W. The on-site corrections are repulsive and correct the d-states by respectively 3.32, 3.7, 5.3, 3.9, 4.38, 6.2, 3.25, and 6.2 eV. A cutoff of 520 eV is applied to the planewaves, and Γ-centered k-point grids with a uniform density of 1000 k-points per reciprocal atom are used to sample the Brillouin zone. We start from the cubic garnet structures of space group #230, and all forces are converged to less than 0.005 eV/Å.

All calculations are performed with spin-polarization, starting from a ferromagnetic ground state as is customary in high-throughput searches. Unfortunately, this means that, in most cases, antiferromagnetic or ferrimagnetic systems will converge to an incorrect ferromagnetic ground state. This is important, in our context, particularly for ferrimagnetic garnets having a 3d

transition metal such as Fe, Ni, Co, Cr, Mn, or V in the B position. We note that not only the spin-state of these garnets but also of anti- and ferrimagnetic systems on the convex hull are treated incorrectly. Consequently, the estimation of E_{hull} for ferrimagnetic garnets is far less accurate than for non-magnetic ones. For example, the experimentally known $Gd_3Fe_5O_{12}$ is predicted to be >1 eV above the hull according to the Materials Project database[26], a value that is certainly grossly overestimated.

To properly estimate E_{hull} for the ferrimagnetic garnets would require obtaining the correct magnetic ordering for a portion of the convex hull as well as for the garnets. This is a complex and computationally expensive task, that is well beyond the scope of this work. Therefore, we made the choice to restrict our discussion to systems not containing the 3d metals mentioned above in the B-site.

It is well-known that the electronic band gaps calculated with the PBE functional are severely underestimated[39]. Therefore, to obtain a more reliable estimation of this important physical property we performed calculations with the modified Becke-Johnson (mBJ) approximation[40], as this is by now recognized as one of the most accurate functional for this task[41].

To calculate the averaged carrier effective masses from the interpolated eigenvalues we follow the approach of ref. [42]. Considering a temperature of 300 K, we deduce the chemical potential required to reach a reference carrier concentration ($10^{18}\,cm^{-3}$) by using BOLTZTRAP2[43,44]. We use a k-point mesh with a regular density of 2000 k-points per reciprocal atom and interpolated the calculated eigenvalues using BOLTZTRAP2[43,44]. The calculated averaged carrier effective masses can be seen as the intrinsic tendency for creating mobile charge carriers in materials[42].

DATA AVAILABILITY
The dataset is available through materials cloud archive materialscloud:2022.107.

CODE AVAILABILITY
The code for CGATs is freely available at https://github.com/hyllios/CGAT.

REFERENCES
1. Yoder, H. & Keith, M. Complete substitution of aluminum for silicon: the system $3MnO \cdot Al_2O_3 \cdot 3SiO_2 — 3Y_2O_3 \cdot 5Al_2O_3$. *Am. Mineral.* **36**, 519–533 (1951).
2. Bertaut, F. & Forrat, F. Structure of ferrimagnetic rare-earth ferrites. *CR Acad. Sci* **242**, 382 (1956).
3. LeCraw, R. C., Spencer, E. G. & Porter, C. S. Ferromagnetic resonance line width in yttrium iron garnet single crystals. *Phys. Rev.* **110**, 1311–1313 (1958).
4. Palik, E. D. *Handbook of Optical Constants of Solids*, vol. 3 (Academic press, 1998).
5. Luke, A. M., Mathew, S., Altawash, M. M. & Madan, B. M. Lasers: A review with their applications in oral medicine. *J Lasers Med Sci.* **10**, 324 (2019).
6. Basavad, M., Shokrollahi, H., Ahmadvand, H. & Arab, S. Structural, magnetic and magneto-optical properties of the bulk and thin film synthesized cerium- and praseodymium-doped yttrium iron garnet. *Ceram. Int.* **46**, 12015–12022 (2020).
7. Sedmidubský, D. et al. Magnetism and optical properties of $Yb_3Al_5O_{12}$ hosted Er^{3+} – experiment and theory. *J. Alloys Compd.* **810**, 151903 (2019).
8. Wako, A. H., Dejene, F. B. & Swart, H. C. Effect of Ga^{3+} and Gd^{3+} ions substitution on the structural and optical properties of Ce^{3+}-doped yttrium aluminium garnet phosphor nanopowders. *Luminescence* **31**, 1313–1320 (2016).
9. Liu, J. & Vohra, Y. K. Sm:YAG optical pressure sensor to 180 GPa:calibration and structural disorder. *Appl. Phys. Lett.* **64**, 3386–3388 (1994).
10. Harris, V. G. Modern microwave ferrites. *IEEE Trans. Magn.* **48**, 1075–1104 (2012).
11. Sayetat, F. Huge magnetostriction in $Tb_3Fe_5O_{12}$, $Dy_3Fe_5O_{12}$, $Ho_3Fe_5O_{12}$, $Er_3Fe_5O_{12}$ garnets. *J. Magn. Magn. Mater.* **58**, 334–346 (1986).
12. Gavriliuk, A. G., Struzhkin, V. V., Lyubutin, I. S. & Trojan, I. A. Irreversible electronic transition with possible metallization in $Y_3Fe_5O_{12}$ at high pressure. *JETP Lett.* **82**, 603–608 (2005).
13. Metselaar, R. & Larsen, P. High-temperature electrical properties of yttrium iron garnet under varying oxygen pressures. *Solid State Commun.* **15**, 291–294 (1974).
14. Wu, M. & Hoffmann, A. Recent advances in magnetic insulators-from spintronics to microwave applications (2013).
15. Subramanian, K. et al. A brief review of recent advances in garnet structured solid electrolyte based lithium metal batteries. *J. Energy Storage* **33**, 102157 (2021).
16. Kim, A., Woo, S., Kang, M., Park, H. & Kang, B. Research progresses of garnet-type solid electrolytes for developing all-solid-state li batteries. *Front. Chem.* **8**, 468 (2020).
17. Schmidt, G., Hauser, C., Trempler, P., Paleschke, M. & Papaioannou, E. T. Ultra thin films of yttrium iron garnet with very low damping: A review. *Phys. Status Solidi B* **257**, 1900644 (2020).
18. Althammer, M. Pure spin currents in magnetically ordered insulator/normal metal heterostructures. *J. Phys. D: Appl. Phys.* **51**, 313001 (2018).
19. Serga, A. A., Chumak, A. V. & Hillebrands, B. YIG magnonics. *J. Phys. D: Appl. Phys.* **43**, 264002 (2010).
20. Ye, W., Chen, C., Wang, Z., Chu, I.-H. & Ong, S. P. Deep neural networks for accurate predictions of crystal stability. *Nat. Commun.* **9**, 3800 (2018).
21. Grew, E. S. et al. Nomenclature of the garnet supergroup. *Am. Mineral.* **98**, 785–811 (2013).
22. Schmidt, J., Pettersson, L., Verdozzi, C., Botti, S. & Marques, M. A. L. Crystal graph attention networks for the prediction of stable materials. *Sci. Adv.* **7**, eabi7948 (2021).
23. Schmidt, J. et al. Predicting the thermodynamic stability of solids combining density functional theory and machine learning. *Chem. Mater.* **29**, 5090–5103 (2017).
24. Oliynyk, A. O. et al. High-throughput machine-learning-driven synthesis of full-heusler compounds. *Chem. Mater.* **28**, 7324–7331 (2016).
25. Fukuda, M., Zhang, J., Lee, Y.-T. & Ozaki, T. A structure map for AB_2 type 2D materials using high-throughput DFT calculations. *Mater. Adv.* **2**, 4392–4413 (2021).
26. Jain, A. et al. The materials project: A materials genome approach to accelerating materials innovation. *APL Mater.* **1**, 011002 (2013).
27. Bergerhoff, G. & Brown, I. *Crystallographic Databases* (International Union of Crystallography, Chester, England, 1987).
28. Schmidt, J., Wang, H.-C., Schmidt, G. & Marques, M. A. L. Machine learning guided high-throughput search of non-oxide garnets. *Materials Cloud* https://arxiv.org/abs/2208.13742 (2022).
29. Schmidt, J. et al. Large-scale machine-learning-assisted exploration of the whole materials space https://arxiv.org/abs/2210.00579 (2022).
30. Ward, L. et al. Matminer: An open source toolkit for materials data mining. *Comput. Mater. Sci.* **152**, 60–69 (2018).
31. Talley, K. R., Perkins, C. L., Diercks, D. R., Brennecka, G. L. & Zakutayev, A. Synthesis of $LaWN_3$ nitride perovskite with polar symmetry. *Science* **374**, 1488–1491 (2021).
32. Kloß, S. D., Weidemann, M. L. & Attfield, J. P. Preparation of bulk-phase nitride perovskite $LaReN_3$ and topotactic reduction to $LaNiO_2$-type $LaReN_2$. *Angew. Chem. Int. Ed.* **60**, 22260–22264 (2021).
33. Sarmiento-Pérez, R., Cerqueira, T. F. T., Körbel, S., Botti, S. & Marques, M. A. L. Prediction of stable nitride perovskites. *Chem. Mater.* **27**, 5957–5963 (2015).
34. Flores-Livas, J. A., Sarmiento-Pérez, R., Botti, S., Goedecker, S. & Marques, M. A. L. Rare-earth magnetic nitride perovskites. *J. Phys.: Mater.* **2**, 025003 (2019).
35. Goodall, R. E. A. & Lee, A. A. Predicting materials properties without crystal structure: deep representation learning from stoichiometry. *Nat. Commun.* **11**, 6280 (2020).
36. Liew, S. S., Khalil-Hani, M. & Bakhteri, R. Bounded activation functions for enhanced training stability of deep neural networks on visual pattern recognition problems. *Neurocomputing* **216**, 718–734 (2016).
37. Blöchl, P. E. Projector augmented-wave method. *Phys. Rev. B* **50**, 17953–17979 (1994).
38. Perdew, J. P., Burke, K. & Ernzerhof, M. Generalized gradient approximation made simple. *Phys. Rev. Lett.* **77**, 3865 (1996).
39. Borlido, P. et al. Large-scale benchmark of exchange–correlation functionals for the determination of electronic band gaps of solids. *J. Chem. Theory Comput.* **15**, 5069–5079 (2019).
40. Tran, F. & Blaha, P. Accurate band gaps of semiconductors and insulators with a semilocal exchange-correlation potential. *Phys. Rev. Lett.* **102**, 226401 (2009).
41. Borlido, P. et al. Exchange-correlation functionals for band gaps of solids: benchmark, reparametrization and machine learning. *Npj Comput. Mater.* **6**, 96 (2020).
42. Hautier, G., Miglio, A., Ceder, G., Rignanese, G.-M. & Gonze, X. Identification and design principles of low hole effective mass p-type transparent conducting oxides. *Nat. Commun.* **4**, 2292 (2013).
43. Madsen, G. K. & Singh, D. J. Boltztrap. a code for calculating band-structure dependent quantities. *Comput. Phys. Commun.* **175**, 67–71 (2006).
44. Madsen, G. K., Carrete, J. & Verstraete, M. J. BoltzTraP2, a program for interpolating band structures and calculating semi-classical transport coefficients. *Comput. Phys. Commun.* **231**, 140–145 (2018).

AUTHOR CONTRIBUTIONS

J.S. developed and trained the machine learning model and made predictions based on it. M.A.L.M and H-C.W. performed the DFT calculations. M.A.L.M and G.S. designed the research. All authors contributed to the analysis and the writing of the manuscript.

COMPETING INTERESTS

The authors declare no competing interests.

ADDITIONAL INFORMATION

Supplementary information The online version contains supplementary material available at https://doi.org/10.1038/s41524-023-01009-4.

Correspondence and requests for materials should be addressed to Miguel A. L. Marques.

Reprints and permission information is available at http://www.nature.com/reprints

Publisher's note Springer Nature remains neutral with regard to jurisdictional claims in published maps and institutional affiliations.